Chapter 6

Experimental realization of non-trivial *Type-II* Dirac cone in InBi

6.1 Introduction

The exotic band structure of topological materials has become an exciting field of inquiry nowadays due to the variety of electronic structures across different members of the family. E.g., in the case of a topological insulator (TI), the surface is protected by time reversal symmetry whereas the bulk remains in insulating phase[85]. The Dirac semi-metals, Weyl semi-metals, *etc.*, on the contrary, have non-trivial bulk Dirac cone[86]. These semi-metals also possess nodal points in them which are the touching points of their valence and conduction bands in the momentum space. The nodal structures (*i.e.*, the loci of nodal points in momentum space) of different topological materials discovered so far are quite rich with some newly discovered compounds within the family showing more complex structures. Thus, we have either a nodal line[30], nodal chain[28], nodal knot[87], nodal-link[88]–[90] or nodal-net[91], [92], *etc.* denoting the richness of the underlying phenomena among them. Few of the recently discovered promising nodal line materials are ZrSiX (X= S, Se, Te)[93], [94], Ag_2S[95], AX_2 (A = Ca, Sr, Ba; X = Si, Ge, Sn).[96], Ca_3P_2[97], CaP_3[98], CaTe[99], CaAuAs[100], CaAgX (X = P, As)[101], IrF_4[28], Mg_3Bi_2[102], XB_2 (X = Ti, Zr)[103], $SrAs_3$[104], Co_2TiX (Si, Ge or Sn)[105],

Ta_3X (X = Al, Ga, Sn, Pb)[106], X_2Y (X = Ca, Sr, Ba; Y = As, Sb, Bi)[107], $YCoC_2$[108], MnN[109] and YH_3[110] *etc*. As the number of electronic states at the nodes in a nodal line system is more than that for a nodal point system, these compounds display various novel properties like large spin Hall effect[111], long-range Coulomb interaction[112], and flat Landau level[113] *etc*. Quite interestingly, the effect of spin orbit coupling on its electronic structure is such that either the nodal line remains protected by some symmetry of the system like *e.g*. inversion symmetry, reflection symmetry, non-symmorphic symmetry, *etc.* or the nodal line gets destroyed by virtue of a gap formation resulting from the lack of such a protection[29], [30], [91], [114], [115]. For instance, the reflection symmetry of the Ta atomic plane protects the nodal line in XTaSe2 (X = Pb, Tl)[116], [117]. In the case of Cu3PdN, nodal lines are protected by the inversion symmetry[92]. For ZrSiS[93] and InBi[118] the nodal lines are protected by non-symmorphic symmetry. Although a vast amount of study has already been done on ZrSiS, InBi remains the least studied compound till date. InBi has two distinct nodal lines protected by non-symmorphic symmetry[118] and it also has a topologically non-trivial *type-II* Dirac cone protected by four-fold cyclic symmetry[118]. Although the nodal lines are verified experimentally earlier[118], the symmetry protected non-trivial Dirac cone is not realized experimentally till date. In the current study, we try to verify the non-trivial Dirac cone by photon energy dependent ARPES study.

6.2 Experimental details and theoretical methods

We prepared a single crystal of InBi using the modified Bridgman method. Elemental In (Alfa Aesar) and Te (Alfa Aesar), with 99.9% purity, have been used as the starting materials. The stoichiometric amount of starting materials were taken in an evacuated (10^{-6} mbar) quartz ampoule. The ingots were then melted at 200° C in the quartz ampoule and kept for 24 hrs at that temperature. The molten ingots were subsequently cooled to 150° C with a cooling rate of 20° hr^{-1}. Thereafter we cooled the molten material from 150° C to 30° C at a slow cooling rate of 3° hr^{-1}. As the bottom of the quartz tube is of a conical shape, the nucleation process starts from the bottommost point of the quartz tube.

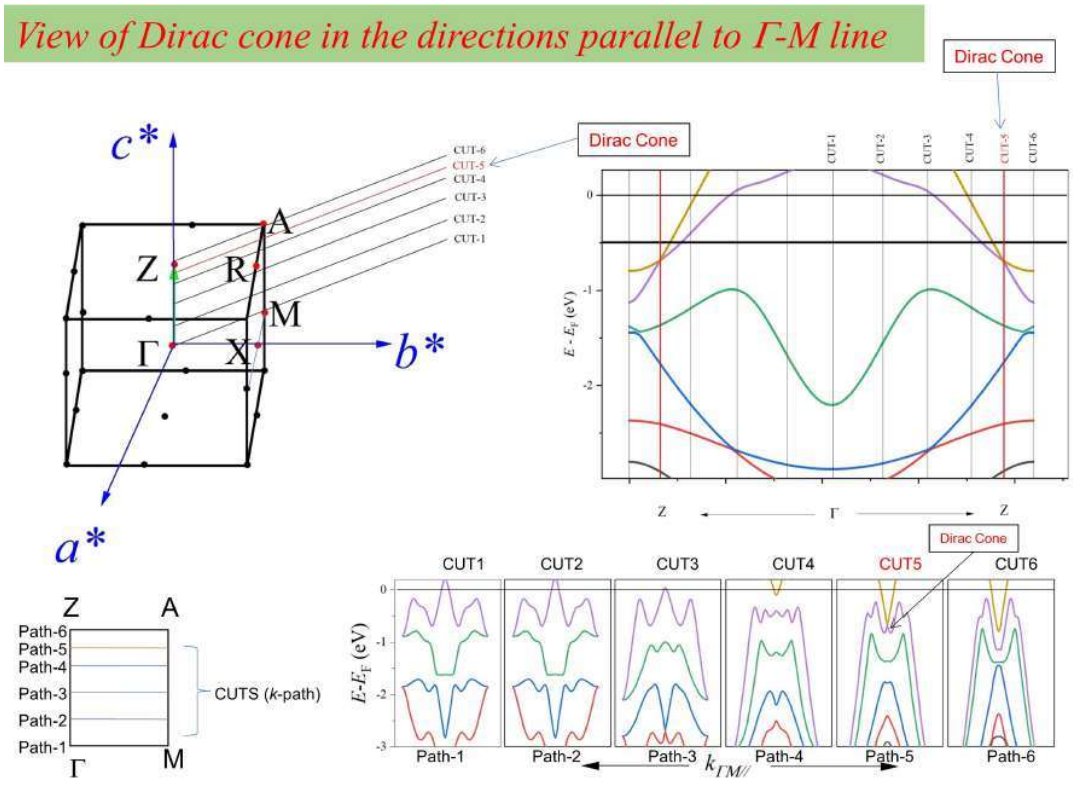

Figure 6.1: (Upper left) The BZ of InBi indicating the high symmetry points. (Upper right) The symmetry protected *type-II* Dirac cone along Γ–*Z* line. (Lower right) The evolution of bands parallel to the Γ–*M* direction with the variation of k_z

Shiny conical shaped single crystals are thus obtained from the quartz tube. Small parts of the crystal have been used for further characterization.

X-ray diffraction (XRD) of a powdered compound was performed for the structural analysis. Further, we also performed XRD on the compound's cleaved surface to check its single crystallinity. The XRD results from the cleaved surfaces identifies various crystallographic planes with respect to their Miller indices. Only reflections from planes of a certain Miller indices and their multiples were observed thus certifying the single crystallinity of the surface.

In order to interpret our experimental results, we have carried out density functional theory calculations using full potential linearized augmented plane-wave based method implemented in the WIEN2k code[122]. All the calculations were performed in a non-spin polarized set-up with a generalized gradient approximation (GGA)[123] approach for the exchange-correlation functional. The spin-orbit coupling is included using a second-variational scheme and thus all the reported results are from GGA+SOC calculations. In order to obtain a very accurate Fermi energy (E_{F}), $R_{mt}K_{max}$ value is considered to be 7 and Brillouin zone (BZ) integration is done using tetrahedron method[124] with a sufficiently dense *k*-mesh ($14 \times 14 \times 14$).

6.3 Result and discussion

The full BZ indicating high symmetry point of InBi is shown in Fig. 6.1. *Type-II* Dirac cones protected by *C4* symmetry lie along the $\Gamma - Z$ axis. The tilted Dirac cone (along $\Gamma - Z$ direction) is indicated by the violet and yellow coloured line. Only these two bands are the prime interest of our study. To observe the energy dispersion of these bands along $\Gamma - M$, we again run the DFT along the aforementioned direction. The band Dispersion along several parallel directions of $\Gamma - M$ are shown by different cuts in Fig. 6.1. We follow the different color codes for the different band dispersion, e.g., the color of a particular band is fixed for the $\Gamma - Z$ and $\Gamma - M$ direction. From the figure, it clearly indicates that the Dirac point lies along *Cut 5* direction. The band dispersion with variation of k_z are shown

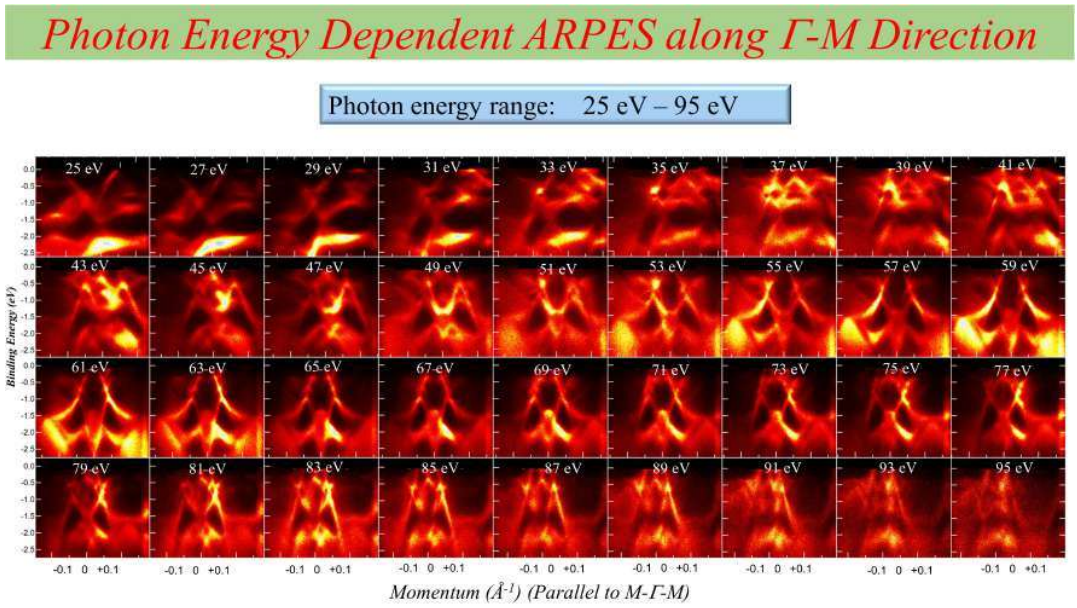

Figure 6.2: Photon energy dependent ARPES spectra parallel to the high symmetry line *M*–Γ–*M*

by different cuts in FIG 6.1.

To probe the Dirac cone experimentally we must perform the k_z dispersion of the above bands. So, we start our experiment with photon energy dependent synchrotron ARPES with 25–95 eV energy range. The whole energy dispersion spectrum is shown in Fig. 6.2. The Band dispersion along *cut 1*, *cut 5* and *cut 6* are shown in Fig. 6.3. We have also put our DFT generated result on the top of the experimental result for the comparison. Our experimental band structure is finely matched with the theoretically generated results. The experimental band structure along *cut 5* also indicates the Dirac point clearly. The 2D dirac cone in the $k_x - k_y$ plane at *cut 5* are also shown in Fig. 6.3. We have shown the anisotropic nature of the Dirac cone in Fig. 6.4. The left panel of the figure indicates the 2D dispersion of the dirac cone in $k_x - k_y$ (at *cut 5*) plane which looks type-I (not tilted) like dispersion, whereas right panel indicates the energy dispersion along $\Gamma Z - \Gamma M$ plane which looks *typ-II* like (tilted) feature. The band dispersion of the Dirac cone near Dirac point is indicated by an orange circle. We have also calculated the surface state (Fig. 6.5) to verify the surface contribution of our experimental band structure. The surface state indicates that the Dirac cone observed in the experiment purely comes from the bulk state. The location of the bulk Dirac cone is indicated by a green circle. Within this circle no

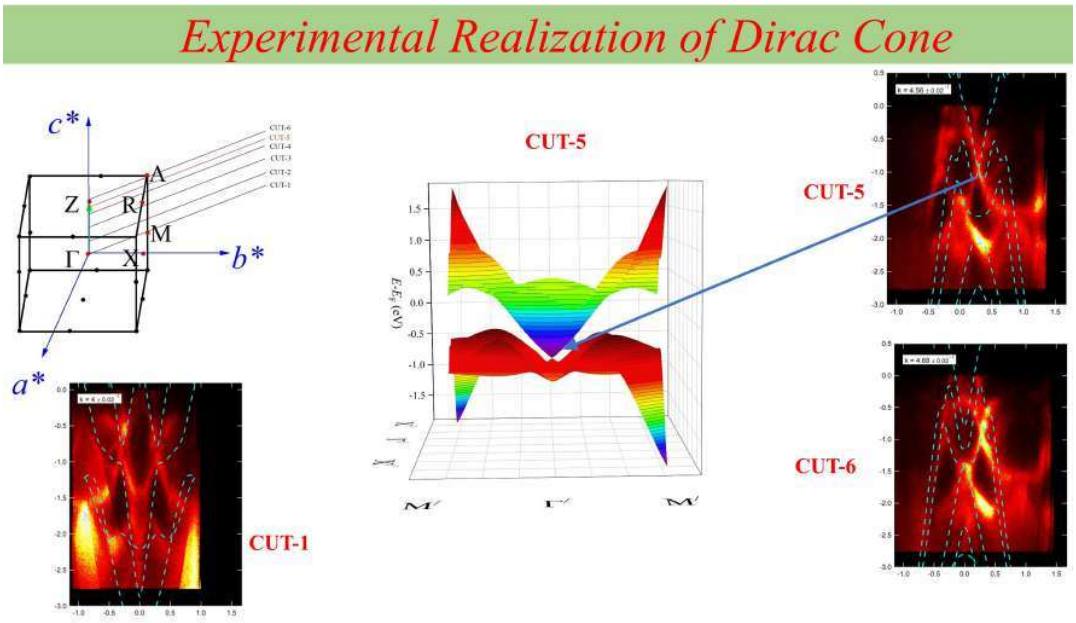

Figure 6.3: Extracted band structure for the particular k-path. The DFT generated band structure are shown by the dashed line. (Centre) The DFT generated 2D Dirac cone (lies parallel to *cut 5*)

surface Dirac cone is observed. The result indicates that our experiment clearly verified the bulk Dirac cone.

Near the Fermi level the bands in InBi are mainly contributed by Bi p orbitals [149] similar to that of AMgBi (A = K, Mg, Cs) systems [150]. In the basis of $|P^+, 1/2\rangle$, $|P^-, 3/2\rangle$, $|P^+, -1/2\rangle$, $|P^-, -3/2\rangle$ the $k.p$ Hamiltonian for the system up to $O(k^2)$ terms can be written as [150]–[152]

$$H_0 = \epsilon_0(k) + \begin{pmatrix} M(k) & Ak_+ & 0 & 0 \\ A(k_- & -M(k) & 0 & 0 \\ 0 & 0 & M(k) & -Ak_- \\ 0 & 0 & -A(k_+ & -M(k) \end{pmatrix}, \tag{6.1}$$

where $\epsilon_0(k) = C_0 + C_1{k_z}^2 + C_2({k_x}^2 + {k_y}^2)$, $M(k) = M_0 - M_1{k_z}^2 - M_2({k_x}^2 + {k_y}^2)$ and $k_\pm = k_x \pm ik_y$. The eigenvalues of H_0 can be written as

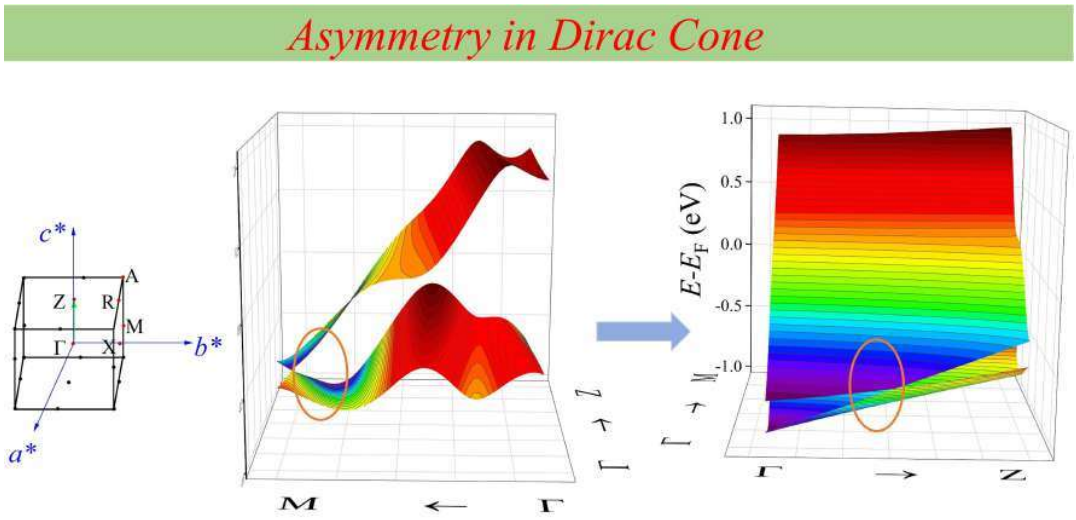

Figure 6.4: (Left panel) Schematic of BZ indicating high symmetry points. (Middle panel) 2D dispersion of the Dirac cone in k_x–k_y plane (along *cut 5*). The symmetric energy–dispersion near Dirac point is indicated by the orange circle, (Right panel) the energy dispersion along Γ–*Z*—Γ–*M* plane. The asymmetric energy–dispersion near Dirac point is indicated by the orange circle

$$E_{\pm}(k) = \epsilon_0(k) \pm \sqrt{M(k)^2 + A({k_x}^2 + {k_y}^2)} = \epsilon_0(k) \pm \sqrt{M(k)^2 + Ak_+k_-}.$$

We obtain two two-fold degenerate bands. By fitting the energy spectra obtained from this effective $k.p$ model with those from the density functional theory calculation, we get the model parameters $C_0 = 0.892$, $C_1 = -4.468$, $M_0 = -0.646$, $M_1 = -1.8125$. Let us consider the four-fold degenerate points along ΓZ line ($k_x = k_y = 0$), which occur at Γ' $(0, 0, \pm k_z^0)$. At these points, $E_+ = E_-$, i.e., $\sqrt{M(k)^2 + Ak_+k_-} = 0$. This enables us to write $k_z^0 = \sqrt{M_0/M_1} = 0.597^{-1}$.

To find the nature of this Dirac point, we need to look at the dispersion of the bands in its vicinity. The 4×4 Hamiltonian in Equation (6.1) can be decoupled into two 2×2 block diagonal matrices. These two 2×2 matrices correspond to the two Weyl points with opposite chirality. We can consider one of the blocks in H_0. We expand $\mathbf{k} = (0 + \delta_x, 0 + \delta_y, k_z^0 + \delta_z)$. Near k_z^0, the effective Hamiltonian to linear order in δ takes the form

$$H' = \begin{pmatrix} 2C_1k_z^0\delta_z - 2M_1k_z^0\delta_z & A(\delta_x + i\delta_y) \\ A(\delta_x - i\delta_y) & 2C_1k_z^0\delta_z + 2M_1k_z^0\delta_z \end{pmatrix}, \tag{6.2}$$

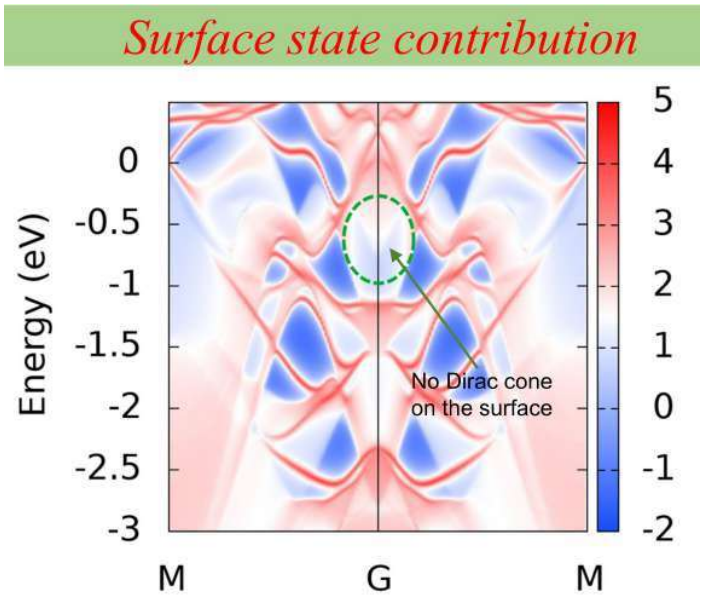

Figure 6.5: The surface state of InBi along *M*–Γ–*M* direction. The green circle indicates the position of bulk Dirac cone

$$= 2C_1 k_z^0 \delta_z \sigma_0 - 2M_1 k_z^0 \delta_z \sigma_z + A\delta_x \sigma_x - A\delta_y \sigma_y. \tag{6.3}$$

This Hamiltonian H' has eigenvalues

$$E'_{\pm} = 2C_1 k_z^0 \delta_z \sigma_0 \pm \sqrt{(2M_1 k_z^0 \delta_z)^2 + A^2({\delta_x}^2 + {\delta_y}^2)} = T(k) \pm U(k).$$

Here $T(k)$ term is linear in momentum and causes a tilt in the spectrum which breaks the Lorentz invariance. The nature of the Dirac point can be categorized depending on the strength of the terms $T(k)$ and $U(k)$. If for any direction $|T(k)| > |U(k)|$, the dispersion becomes anisotropic, resulting in a *type-II* Dirac point [153]. For our system under consideration, from fitted parameters, we find that $|C_1| > |M_1|$. This means that $|T(k)| > |U(k)|$ along the ΓZ direction ($\delta_x = \delta_y = 0$ along this direction) making the tilt large enough. Thus, we can conclude that the Dirac point under consideration is indeed a *type-II* Dirac point.

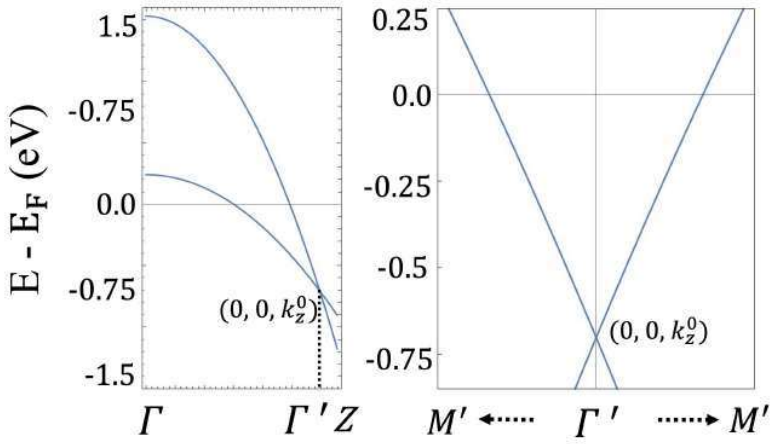

Figure 6.6: Band dispersions obtained from low energy $k.p$ model. Electronic spectra obtained from the low energy $k.p$ model for InBi along (left) Γ–*Z* and (right) *M'*–Γ*'*–*M'* (parallel to *M*–Γ–*M* and *A*–*Z*–*A*) direction.

6.4 Conclusion

The non-trivial *type-II* Dirac cone protected by *C4* symmetry in the nodal line semimetal InBi is verified experimentally. The experimental band structure from the ARPES study excellently matches the theoretically generated results. The nature of the Dirac cone is anisotropic e.g., it looks symmetric or asymmetric (tilted) nature with the variation of *k*-path. The anisotropic nature of Dirac cone is further verified from the low energy $k.p$ model.